uses the same thrust T_0, it will not be able to sustain level flight, but will have to dive at an angle γ such that

$$T_0 + W \sin\gamma = k c_{D2} (U_0 + \delta V_2)^2 \tag{5}$$

resulting in a vertical velocity w_2, which can be shown to be (again assuming small angles) by the earlier procedure

$$w_2 = V_2 \left\{ \left(\frac{c_{D2}}{c_{L2}} \right) \left[1 + \frac{2\delta V_2}{U_0} + \left(\frac{\delta V_2}{U_0} \right)^2 \right] - \left(\frac{c_{D0}}{c_{L_0}} \right) \right\} \tag{6}$$

The loitering maneuver can now be described. The UAV is pointed westward and flown at constant thrust T_0. At times when the oncoming wind is weaker than the nominal speed U_0, the UAV climbs with vertical speed w_1 while staying at the same position in the horizontal plane. On the other hand, when the oncoming windspeed is faster than U_0, the UAV sinks at vertical speed w_2, again staying at the same position in the horizontal plane.

Inspection and comparison of Eqs. (4) and (6) shows that w_2 is always greater than w_1. However, one can always find a speed U_0, for which the percentage of time τ_1 at which winds slower than U_0 blow is larger than that of winds stronger than U_0, τ_2, so that the average vertical excursion can be brought to be zero. Actually, the flight altitude and nominal speed U_0 for a given mission, or parts of it, thus should be chosen according to the local windspeed histogram.

Take as an example, $\delta V_1 = \delta V_2 \equiv \delta V$ and $c_{D2} = c_{D1} = c_{D0}$, which, while admittedly not accurate, allows an algebraically simple solution with no aircraft specific parameters. Then, for zero total vertical excursion,

$$w_1 \tau_1 = w_2 \tau_2 \tag{7}$$

where τ_1 is the time winds are blowing at $U_0 - \delta V$ and τ_2 is the time winds are blowing at $U_0 + \delta V$. From Eq. (7), substituting Eqs. (6) and (4), we obtain for $A \equiv \delta V / U_0$

$$Z = \frac{\tau_2}{\tau_1} = \frac{1 - A}{1 + A} \frac{2A - A^2}{2A + A^2} = \frac{2 - 3A + A^2}{2 + 3A + A^2} \tag{8}$$

The ratio of times required, Z, as a function of the speed excursion A appears in Fig. 2. In conjunction with Fig. 1 or similar data, this can now be used to establish the nominal velocity U_0 for any given area and time of year. Obviously, A should be small so the danger of stall is minimized, but not small enough so that every fluctuation in windspeed causes a change.

To clarify, a numerical example follows based on the specific conditions measured in the Mediterranean area.[4] The worst case in the Mediterranean area is in winter, where[4] at altitudes from 16 to 25 km, the windspeed exceeds 15 m/s 50% of the time, 20 m/s is exceeded 30%, 25 m/s is exceeded 20%, and 37.5 m/s is only reached 2% of the time (see Fig. 1). Thus, taking a nominal true airspeed for the aircraft of $U_0 = 32.5$ m/s we obtain, by interpolation, that dives will be required less than 6% of the time. On the other hand, taking an excursion in speed of 5 m/s (i.e., $A = \frac{5}{32.5} = 0.15$, approximately), we again obtain from the data that windspeeds will be in the range

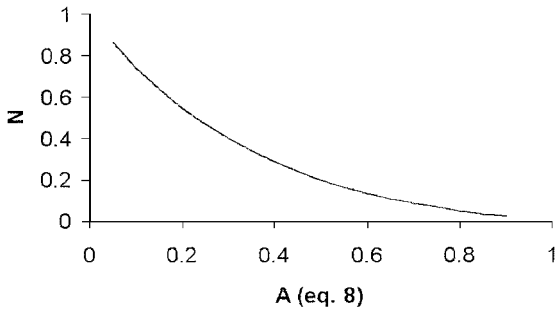

Fig. 2 Ratio of times required Z vs the normalized speed difference A, see Eq. (8).

27.5–32.5 m/s about 9% of the time. From Fig. 2, we see that for $A = 0.15$, $\tau_2/\tau_1 = 0.64$, which converges within 1% with the values obtained from Fig. 1.

Conclusion

Obviously, this loitering maneuver will need further tuning for specific cases using the full Eqs. (4) and (6). For hybrid and fully fueled long-endurance UAVs, the design point will also require adjustment for the reduction in weight due to fuel consumption during the mission, but this is shared with all other maneuvers mentioned and easily overcome.

References

[1] Brandt, S. A., and Gilliam, F. T., "Design Methodology for Solar Powered Aircraft," *Journal of Aircraft*, Vol. 32, No. 4, 1995, pp. 703–709.

[2] Youngblood, J. W., Talay, T. A., and Pegg, R. J., "Design of Long Endurance, Unmanned Airplanes Incorporating Solar and Fuel Cell Propulsion," AIAA Paper 84-1430, June 1984.

[3] Harmats, M., and Weihs, D., "Hybrid Propulsion, High Altitude Long Endurance Remotely Piloted Vehicle," *Journal of Aircraft*, Vol. 36, No. 2, 1999, pp. 321–331.

[4] Stragnac, T. W., "Wind Study for High Altitude Platform Design," NASA RP-1044, 1979.

[5] Morris, C. E. K., Jr., "Microwave Powered Unmanned High Altitude Airplanes," *Journal of Aircraft*, Vol. 21, No. 6, 1984, pp. 966–970.

[6] Ito, T., "A Practical Flight Path for Microwave Powered Airplanes," *Transactions of the Japan Society for Aeronautical and Space Sciences*, Vol. 32, No. 98, 1990, pp. 226–231.

Baseline Validation of Unstructured Grid Reynolds-Averaged Navier–Stokes Toward Flow Control

Ronald D. Joslin*
Pennsylvania State University, State College, Pennsylvania 16804
and
Sally A. Viken†
NASA Langley Research Center, Hampton, Virginia 23681

I. Introduction

THE value of the use of the Reynolds-averaged Navier–Stokes methodology for active flow control applications is assessed. An experimental flow control database exists for a NACA0015 airfoil modified at the leading edge to implement a fluidic actuator; hence, this configuration is used. Computational results are documented for the baseline wing configuration (no control) with the experimental results and assumes two-dimensional flow. The baseline wing configuration has discontinuities at the leading edge, trailing edge, and aft of midchord on the upper surface.

A limited number of active flow control applications have been tested in the laboratory and in flight. These applications include dynamic stall control using a deformable leading edge,[1] separation control for takeoff and landing flight conditions using piezoelectric devices,[2,3] pulsed vortex generators,[4] zero-net-mass oscillations,[5,6]

Received 16 June 2000; revision received 27 November 2000; accepted for publication 28 November 2000.

*Deputy Head, Applied Research Laboratory, Computational Modeling and Control Department, P.O. Box 30. Senior Member AIAA.

†Aerospace Engineer, Flow Physics and Modeling Department, Mail Stop 170.

and thrust vectoring with zero-net-mass piezoelectric-driven oscillatory actuation.[7]

As yet, there is no definitive comparison with experimental data that indicates current computational capabilities can quantitatively predict the large aerodynamic performance gains achieved with active flow control in the laboratory. However, one study[8] using the Reynolds-averaged Navier–Stokes (RANS) methodology has shown good quantitative agreement with experimental results for an isolated zero-net-mass actuator. In addition, some recent studies[9,10] have used RANS to demonstrate qualitative performance gains compared with the experimental data for separation control on an airfoil. Those quantitative comparisons for both baseline and flow control cases indicated that computational results were in poor quantitative agreement with the experiments.

The current research thrust will investigate the potential use of an unstructured grid RANS approach to predict aerodynamic performance for active flow control applications building on the early studies.[9,10] First the computational results must quantitatively match experiments for the no-control case before proceeding to the time-dependent flow control case. This paper documents the baseline (no-control) case using an unswept airfoil configuration.

The next section describes the configurations used for the computations and the experimentals. The computational approach is then described followed by results and concluding remarks.

II. Airfoil Configurations and Experimental Data

Figure 1 shows the leading-edge and trailing-edge regions of the configurations used in the present study. The midchord regions for all airfoils are the same and, therefore, not shown in Fig. 1. A NACA0015 airfoil is used in the study to provide reference point results. The finite thick trailing edge of the NACA0015 airfoil matches the TAU0015. The TAU0015 airfoil model was tested in a low-speed wind tunnel at the Tel Aviv University (TAU). The model is a NACA0015 airfoil modified in the leading-edge region to acommodate an actuation slot. Hence, the airfoil configuration is referred to as the TAU0015 airfoil. The TAU0015 model has a 0.3645-m chord, a 0.3% thick blunt trailing edge, and a 0.4% chord thick notch at 76.6% chord, which results from the flap/main element connection used in a different experiment. The actuator for the TAU0015 tests was located at the leading edge and leads to the 0.3% chord discontinuity (straight horizontal line region).

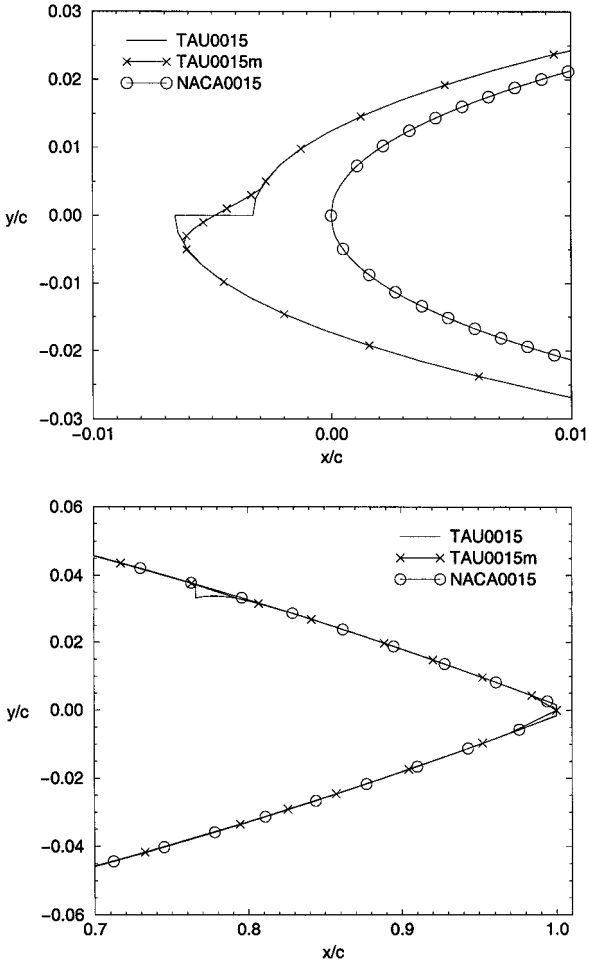

Fig. 1 NACA0015, TAU0015, and TAU0015m airfoils.

The previous computational studies[9,10] used single-block structured grid RANS and for convenience ignored the 76.6% chord notch and trailing-edge thickness and faired over (smoothed) the leading-edge discontinuity. Here, this altered configuration is referred to as TAU0015m; computational results from this model will be compared with the TAU0015 configuration. There is no experimental data for the numerically modified model.

The flow control experiments with the TAU0015 were conducted in the Meadow–Knapp Low Speed Wind Tunnel at the TAU.[5] The test section is 1.50 m high and 0.61 m wide. The TAU0015 model was instrumented with 36 static pressure taps, and measurements were made using a Scanivalve and a pressure transducer, 5 psi full scale. The transducer has an accuracy of 0.06% full scale. The freestream velocity of all tests was nominally 51 m/s. The pressure coefficient results are accurate to within $\pm 0.6\%$. Lift, Cl, and drag, Cd, coefficients are obtained by integrating the measured pressures; accuracy in Cl is estimated to ± 0.01 for prestall conditions and ± 0.03 poststall. The drag coefficient Cd has experimental uncertainty of ± 0.003 at prestall conditions and and $\pm 10\%$ at poststall conditions. The experimental conditions are at a Mach number of 0.15 and a chord Reynolds numbers of 1.2×10^6. The uncertainty in Reynolds number is $\pm 2\%$ due to variations in temperature and velocity during the tests.

The Cl and Cd for the experimental data are available at angle of attacks α from 0 to 24 deg in 2-deg increments. The maximum lift coefficient is $Cl = 1.056$ at $\alpha = 12$ deg and $Cd = 0.0288$. In addition, pressure coefficients Cp at $\alpha = 8$ and 22 deg are used for the current comparison.

III. Computational Approach

The full unstructured Navier–Stokes two-dimensional RANS code (FUN2D)[11] will be used for the current study. The FUN2D code solves the time-dependent RANS equations expressed as a system of conservation laws relating the rate of change of mass, momentum, and energy in a control volume to the fluxes of these quantities through the control volume. The solver is an implicit, upwind-differencing algorithm with the inviscid fluxes obtained on each face of the control volume with Roe's flux-difference-splitting scheme. The node-based algorithm stores the variables at the vertices of the mesh, and the equations are solved on the nonoverlapping control volumes surrounding each node. The viscous terms use a central difference formulation evaluated with the finite volume formulation. Time advancement is made with a linearized first-order backward Euler scheme. At each time step, the equations are solved with 15 Gauss–Seidel subiteratives, sequentially solving for all odd numbered nodes and then all even numbered nodes. A two-level V-type multigrid approach is used for this baseline study to accelerate convergence.[12] A very fine grid was first used to determine the effect of the geometric discontinuities on the aerodynamic performance. Then grid coarsening was implemented to minimize the grid requirements for accurate results and more efficient computations. The Spalart–Allmaras (SA) turbulence model[13] is used in this investigation, and all computations involve fully turbulent flow. A computer workstation is used for the present study.

The unstructured grids were generated with advancing-front-type point placement with iterative local remeshing for grid quality improvement.[14,15] Figure 2 shows an initial coarse grid around the TAU0015 airfoil, resolving all discontinuities on the configuration. Similar grids were generated for the TAU0015m and NACA0015 airfoils. The grids extend from the airfoils to form a far-field circle with a radius of 20 chord lengths around the airfoils.

Table 1 Number of nodes used for initial computations

Configuration	Grid1 total	Grid1 surface	Grid2 total	Grid2 surface
TAU0015	114,119	1,891	51,150	1,260
TAU0015m	48,063	1,032	21,316	516
NACA0015	62,764	1,100	25,352	550

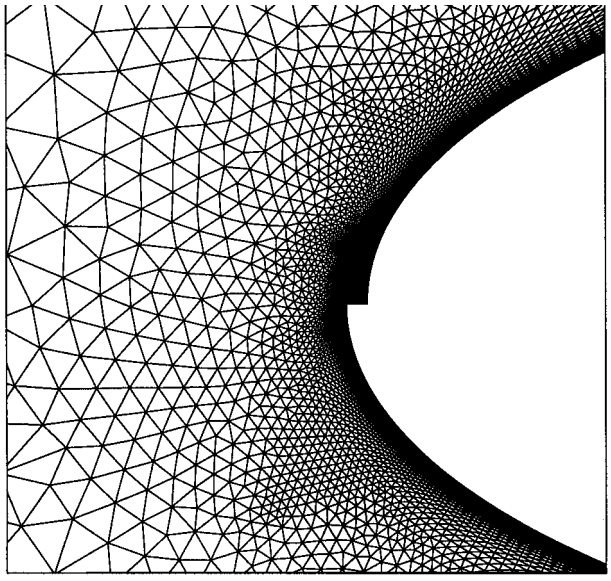

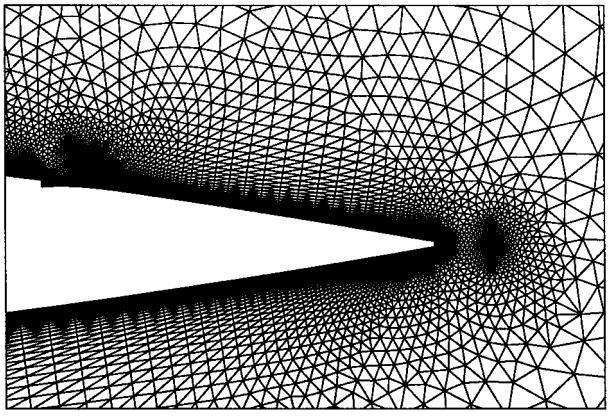

Fig. 2 Coarse grid for TAU0015 airfoil.

IV. Results

All grids in the initial computations had the first near-surface grid point below $y^+ = 0.7$ to ensure the sublayer of the turbulent shear flow was sufficiently resolved. This specification of the first grid point approximation is based on relationships between y^+, Reynolds number, and skin friction for a flat plate boundary layer. For turbulent flow, this relationship yields an analytical relationship between y^+ and the first wall-normal grid point. This relationship is $y^+ = \Delta y \cdot \sqrt{(c_f/2)Re}$, where $c_f \simeq 0.455/\ell n^2(0.06Re_x)$ and Δy is the physical distance for the first grid point away from the airfoil surface. Specifying a midchord $y^+ = 0.102$ will keep all near-wall points below 0.7, as will be shown later.

The number of surface nodes and total grid nodes for the first comparison are shown in Table 1 for each airfoil. The TAU0015 airfoil grid has significantly more grid points because of the grid clustering near the surface discontinuities, which are not present in the TAU0015m and NACA0015 airfoils.

Convergence of the steady-flow computations was achieved when the change in Cl was less than 0.015% per iteration. At this criterion, Cd was changing by less than 0.005% per iteration. The only unsteadiness in the computations was observed at $\alpha = 26$ deg; unsteady vortex shedding was evident.

Figure 3 shows the computed Cl with variation in α for the NACA0015, TAU0015, and TAU0015m airfoils compared with the experimental data. For the NACA0015, the maximum Cl and stall α are 30% and 4 deg higher than the experimental data. For the TAU0015m airfoil, the maximum Cl and stall angle are 23% and 2 deg higher than the experiments. These overpredictions for the TAU0015m airfoil are consistent with the earlier studies,[9,10] which used the same airfoil but a structured grid and two different RANS

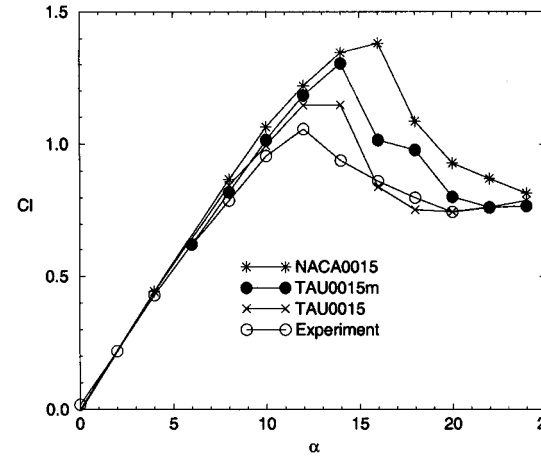

Fig. 3 Computed Cl vs α for TAU0015, TAU0015m, and NACA0015 airfoils compared with experimental data.

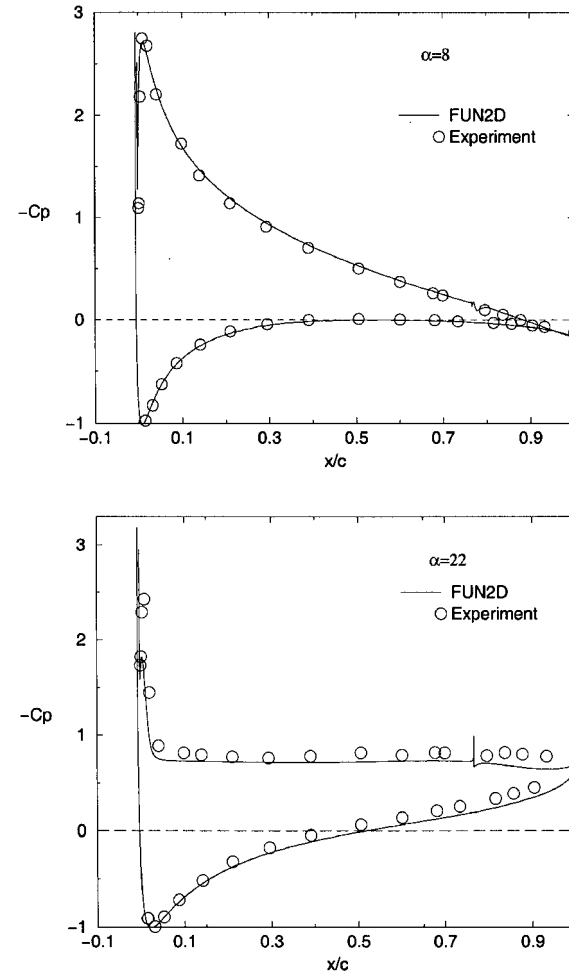

Fig. 4 Computational and experimental pressure coefficients Cp for TAU0015 airfoil at α = 8 deg (prestall) and 22 deg (poststall).

codes. In closer agreement, the computed results for the TAU0015 airfoil approach the experimental results, overestimating the stall angle by 2 deg and the maximum *Cl* by 9%. Thus, the subtle differences in geometry for the NACA0015, TAU0015m, and TAU0015 airfoils have led to large differences in the computed stall α and maximum *Cl*.

A reasonable explanation for the differences between computational and experimental results for the TAU0015 geometry may be obtained with a careful review of the experimental results. In the experiments, *Cl* and *Cd* are derived from numerical integration of the static pressure measurements. Hence, a comparison of computed and measured pressure information is necessary for this review. Figure 4 shows computed pressure coefficients *Cp* for the TAU0015 airfoil compared with experimental results for $\alpha = 8$ deg (prestall) and 22 deg (poststall). The computational results show pressure spikes at the leading edge and near 76% chord resulting from the geometrical discontinuities. No pressure spikes were measured in the wind-tunnel experiments because no taps were or could be positioned on the actuator. Therefore, the experiments could not capture the additional pressure spike predicted in the computations. Based on this understanding of the experimental data, the computed *Cl* and *Cd* are now obtained by integrating the pressure over the TAU0015 airfoil in regions consistent with the experimental pressure taps. Only the contribution from the leading-edge actuator discontinuity are excluded in this new *Cl* and *Cd*. The *Cl* and *Cd* vs α are compared with experimental data in Fig. 5. The computed maximum *Cl* is now overpredicted by 2% compared with the experimental data, and the stall α are in agreement at 12 deg. The overprediction in lift results in an underprediction of the drag. The poststall (separated) conditions show notable disagreement between computational and experimental results. Whereas the SA turbulence model has not been developed or validated for separated flows, significant uncertainty exists in experimental error assessment for separated flow regions. Unless the 36 pressure taps used in the experiments were positioned to capture all of the essential physics of the separated flow, large (unpredictable) uncertainty could exist for the *Cl* and *Cd* values. Such experimental uncertainty for poststall conditions is confirmed in results for a simple NACA0012 airfoil.[16,17] Hence, the computational and experimental results have uncertainty in their respective quantities for highly separated flow conditions.

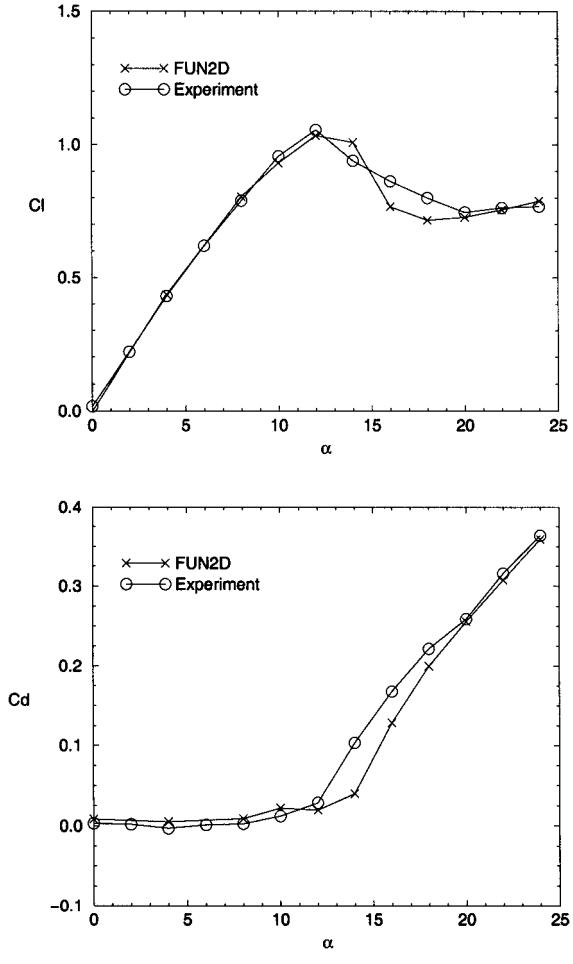

Fig. 5 Computed *Cl* and *Cd* vs α compared with experimental data for TAU0015 airfoil.

In any grid generation process, some judgment must be made concerning the adequacy of the grids for the computations. This is usually facilitated by grid refinement studies. Such a study was carried out but is not reported due to space limitations. The grid refinement analysis confirms the validity of the reported grids.

V. Conclusions

Results from an unstructured-grid RANS code were used to analyze the possible impact of small geometric differences in airfoils on aerodynamic performance. Results for NACA0015, TAU0015, and TAU0015m airfoils were compared with experimental data for the TAU0015 airfoil configuration. The TAU0015 airfoil has discontinuities at the leading edge, trailing edge, and aft of midchord on the upper surface.

The TAU0015m was similar to the TAU0015 except the leading-edge shape was smoothed to make the geometry more continuous and the midchord notch was ignored. The current TAU0015m results are in agreement with previous investigations.

A comparison of the results from the various airfoils suggests that the midchord discontinuity does not affect the aerodynamics of the wing and can be ignored for more efficient computations. The leading-edge discontinuity significantly affects the lift and drag; hence, the integrity of the leading-edge notch discontinuity must be maintained in the computations to achieve a good match with the experimental data.

The analysis of computed performance vs experimental data for the TAU0015 airfoil demonstrated that consistency in determining lift and drag coefficient quantities was important to achieve quantitative agreement. The integration of computed pressure should be contained to regions of the airfoil consistent with the pressure taps.

Future activities for the validation of RANS for active flow control will include an investigation of the accuracy of RANS for time-dependent flow problems, the introduction of boundary conditions to model the oscillatory actuation, and an evaluation of oscillatory excitation on the aerodynamic performance. The oscillatory excitation results will be compared with experiments for the current TAU0015 configuration.

Acknowledgments

The authors are indebted to Avi Seifert, Tel Avi University, for supplying the geometry and experimental data for the TAU0015 model. Also, we are grateful for the use of the FUN2D code developed at NASA Langley Research Center.

References

[1] Chandrasekhara, M. S., Wilder, M. C., and Carr, L. W., "Control of Flow Separation Using Adaptive Airfoils," AIAA Paper 97-0655, Jan. 1997.

[2] Seifert, A., Bachar, T., Wygnanski, I., Kariv, A., Cohen, H., and Yoeli, R., "Application of Active Separation Control to a Small Unmanned Air Vehicle," *Journal of Aircraft*, Vol. 36, No. 2, 1998, pp. 474–477.

[3] Seifert, A., Eliahu, S., Greenblatt, D., and Wygnanski, I., "Use of Piezoelectric Actuators for Airfoil Separation Control," *AIAA Journal*, Vol. 36, No. 8, 1998, pp. 1535–1537.

[4] McManus, K., and Magill, J., "Separation Control in Incompressible and Compressible Flows Using Pulsed Jets," AIAA Paper 96-1948, June 1996.

[5] Seifert, A., Darabi, A., and Wygnanski, I., "Delay of Airfoil Stall by Periodic Excitation," *Journal of Aircraft*, Vol. 33, No. 4, 1996, pp. 691–698.

[6] Seifert, A., and Pack, L. G., "Oscillatory Excitation of Unsteady Compressible Flows over Airfoils at Flight Reynolds Numbers," AIAA Paper 99-0925, Jan. 1999.

[7] Pack, L. G., and Seifert, A., "Periodic Excitation for Jet Vectoring and Enhanced Spreading," AIAA Paper 99-0672, Jan. 1999.

[8] Kral, L. D., Donovan, J. F., Cain, A. B., and Cary, A. W., "Numerical Simulation of Synthetic Jet Actuators," AIAA Paper 97-1824, June 1997.

[9] Donovan, J. F., Kral, J. D., and Cary, A. W., "Active Flow Control Applied

to an Airfoil," AIAA Paper 98-0210, Jan. 1998.
[10]Ravindran, S. S., "Active Control of Flow Separation over an Airfoil," NASA/TM-1999-209838, Dec. 1999.
[11]Anderson, W. K., and Bonhaus, D. L., "An Implicit Upwind Algorithm for Computing Turbulent Flows on Unstructured Grids," *Computers and Fluids*, Vol. 23, No. 1, 1994, pp. 1–21.
[12]Anderson, W. K., Rausch, R. D., and Bonhaus, D. L., "Implicit/Multigrid Algorithms for Incompressible Turbulent Flows on Unstructured Grids," *Journal of Computational Physics*, Vol. 128, 1996, pp. 391–408.
[13]Spalart, P. R., and Allmaras, S. R., "A One-Equation Turbulence Model for Aerodynamic Flows," AIAA Paper 92-0439, Jan. 1992.
[14]Marcum, D. L., "Generation of Unstructured Grids for Viscous Flow Applications," AIAA Paper 95-0212, Jan. 1995.
[15]Marcum, D. L., and Weatherhill, N. P., "Unstructured Grid Generation Using Iterative Point Insertion and Local Reconnection," *AIAA Journal*, Vol. 33, No. 9, 1995, pp. 1619–1625.
[16]McCroskey, W. J., McAlister, K. W., Carr, L. W., and Pucci, S. L., "An Experimental Study of Dynamic Stall on Advanced Airfoil Sections Volume 1. Summary of the Experiment," NASA TM 84245, July 1982.
[17]McCroskey, W. J., "A Critical Assessment of Wind Tunnel Results for the NACA 0012 Airfoil," CP-429, AGARD, 1987.

Modeling of the Receiver Aircraft in Air-To-Air Refueling

A. W. Bloy* and M. M. Khan†
University of Manchester, Manchester, England M13 9PL, United Kingdom

Nomenclature

b	=	wing span, m
C_l	=	rolling moment coefficient, $L/q_\infty Sb$
L	=	rolling moment, Nm
L_{RT}	=	matrix of direction cosines
$Oxyz$	=	axes fixed in aircraft
P, Q, R	=	angular velocity components about Ox, Oy, and Oz, rad s^{-1}
q	=	dynamic pressure, Nm^{-2}
S	=	wing area, m^2
U, V, W	=	velocity components along Ox, Oy, and Oz, ms^{-1}
v	=	resultant velocity, $[U \;\; V \;\; W]^T$, ms^{-1}
y	=	sideways displacement from the plane of symmetry of the tanker wing, positive to starboard, m
z	=	vertical position below tanker wing apex, m
θ	=	pitch angle, rad
ϕ	=	bank angle, rad
ψ	=	yaw angle, rad
∇	=	gradient operator, $[\partial/\partial x \;\; \partial/\partial y \;\; \partial/\partial z]^T$

Subscripts

R	=	receiver aircraft
T	=	tanker aircraft
w	=	(tanker) wake
∞	=	free-flight condition

Superscript

T	=	transpose of matrix

Received 24 June 2000; revision received 1 November 2000; accepted for publication 17 November 2000.

*Lecturer, School of Engineering.
†Research Student, School of Engineering.

Introduction

THERE is active interest in the United Kingdom in setting up a real-time air-to-air refueling flight simulation for training purposes with work carried out by the flight management and control group at the Defence Evaluation Research Agency (DERA), Bedford. The work has initially been aimed at the simulation of the Tornado combat aircraft making contact with the VC10 tanker aircraft and with aerodynamic modeling provided by the present authors. The purpose of this Note is (1) to outline the approximate model of the receiver used in the real-time simulation to reduce computing time and (2) to justify its use by estimating the accuracy of prediction of one of the main aerodynamic effects, namely, the rolling moment induced on the receiver by the tanker wake.

The approximate receiver model adopted is the single-point model as applied by Etkin[1] in the case of wind effects on aircraft. This model is based on the tanker wake conditions at the receiver center of gravity and determines the effect of the tanker wake-induced velocity on the receiver air speed. All six of the translational and rotational air speed components are considered. An advantage of this simple model is that it applies to any receiver aircraft using the aircraft aerodynamic data stored in the flight simulation. To validate the approximate model, the tanker wake and receiver aircraft model developed previously by Bloy and West[2] is used. This model incorporates a line vortex model of the tanker wake rollup with the vortex lattice method applied to all lifting surfaces and with the effect of the tanker wake on the receiver represented by equivalent twist distributions of the lifting surfaces. Linear distributions of downwash and sidewash are assumed in the single-point model compared with variable downwash and sidewash in the exact model.

Tanker Wake Results

The DERA flight simulation required wake velocity data for the VC10 tanker at typical flight conditions corresponding to a flight Mach number of 0.544 and an aircraft lift coefficient of 0.335. As in previous work,[3] the VC10 is represented by its wing planform with the vortex wake rollup calculated to a distance of five wing spans downstream. Over the tanker wing with a downstream step size equal to one-eighth of the wing mean chord, 60 equally spaced spanwise with two chordwise line vortices are taken. To avoid chaotic motion where vortex lines intersect each other, the smoothing factor proposed by Krasny[4] is used with the value of this factor taken as 1% of the wing span.

In the DERA simulation, the wake conditions are specified by a three-dimensional data array giving the downwash and sidewash velocities together with three velocity gradients required in the single-point model described in the following section. Figure 1 shows typical spanwise distributions of downwash velocity at a position one wing span downstream. At this downstream location, which corresponds approximately to the point at which the receiver makes contact with the center hose and drogue, the wake rollup is only partly complete. Figure 1 shows the large gradients of downwash near the tip vortex with the induced flow changing to an upwash outboard of the wing tip.

Single-Point Model of Receiver Aircraft

Etkin[2] considers the aircraft as planar with simple expressions given for the wake-induced roll, pitch, and yaw rates in terms of the velocity gradients over the lifting surfaces. When receiver aircraft axes are used as the frame of reference, the equivalent rotational velocity components of the tanker airwake P_w, Q_w, and R_w are given from Etkin[2] by

$$P_w = \frac{\partial W_w}{\partial y}, \qquad Q_w = \frac{-\partial W_w}{\partial x}$$

$$R_{1w} = \frac{-\partial U_w}{\partial y}, \qquad R_{2w} = \frac{\partial V_w}{\partial x} \tag{1}$$

as shown in Fig. 2. The effective roll, pitch, and yaw rates of the receiver aircraft relative to the air are $(P - P_w)$, $(Q - Q_w)$, and